CHAPTER 13

APPLICATIONS OF HHT IN IMAGE ANALYSIS

Steven R. Long

The recently developed empirical mode decomposition/Hilbert–Huang transform (EMD/HHT) for the analysis of nonlinear and non-stationary data has been extended to include the analysis of image data. Because image data can be expressed in terms of an array of rows and columns, this robust concept is applied to these arrays row by row. Each slice of the data image, either row or column-wise, represents local variations of the image being analyzed. Just as much of the data from natural phenomena are either nonlinear or non-stationary, or both, so are the data that form images of natural processes. Thus, the EMD/HHT approach (or HHT in abbreviated form) is especially well-suited for image data, giving frequencies, inverse distances or wavenumbers as a function of time or distance, along with the amplitudes or energy values associated with these, as well as a sharp identification of embedded structures. The varied products of this new analysis approach are joint and marginal distributions to be viewed as isosurfaces, contour plots, and surfaces that contain information on frequency, inverse wavelength, amplitude, energy and location in time, space, or both. Additionally, component images representing the intrinsic scales and structures embedded in the data will be described, as well as a technique for obtaining frequency variations.

13.1. Introduction

Images have long held a fascination for us, for our eyes constantly input a stream of data into our minds from the world around us, images we process to obtain distance, size, color, orientation, along with beauty or even a sense of danger. We have always analyzed and characterized drawings, inscriptions, and paintings and assigned them a level of value and appreciation accordingly. Our minds are capable of image processing of the highest order.

In recent times, it has become technically possible to obtain images that are more than just a picture, images that are actually an array of numbers of high precision that represent point-wise measurements over an area, not just the gray scale value in a scanned photograph, but a detailed measure of electromagnetic wavelength and intensity representing color, heat, or x-ray intensity, to name just a few, all with underlying physical significance. Images are also routinely acquired from sources other than electromagnetic waves, such as magnetic resonance images. These arrays of numbers are handled easily by computer and can thus be displayed, printed, and viewed as an image, while representing a reality that our own eyes could never see directly. In this sense, modern imaging technology and techniques have expanded our vision, allowing us to "see" new things never observed before. Such is also the case when applying a totally different method to image analysis, a method such as the EMD/HHT technique. New types of results can be expected, allowing our minds to see the reality around us in entirely new ways. In fact, this process has already begun in the many and various applications of EMD/HHT reported to date on "one-dimensional" data such as time records of earthquakes, ocean waves, rogue water waves, sound analysis, and length-of-day measurements. The approach has been successful with nonlinear and non-steady data because its basis functions are time varying and adaptive.

If this data in general can be written as $X(d)$, then the first step in this new approach is to "sift" or decompose the data into n empirical components such that

$$X(d) = \sum_{j=1}^{n} c_j + r_n \,, \tag{13.1}$$

where c_j is the jth component, r_n is the residue, and d denotes the axis over which the data varies, such as time or spatial distance. The sifting stops when either the last component c_n or the residue r_n reaches a value lower than a predetermined level, which is a small value of no consequence, or when r_n becomes a monotonic function from which no more components can be extracted. Even if the data have a zero mean, the final residue can be different from zero. If the data contain a trend (such as a slow drift in the instrument calibration or the tide changing during ocean-wave measurements), then when the sifting is completed, the residue r_n will be that trend.

Just as in earlier work on the EMD/HHT analysis, this sifting will be employed here on data that make up each row or column of an image array. Thus, the initial processing used here is identical with that used in earlier reports. The application to images, however, requires this new sifting processing and subsequent analysis to be repeated perhaps hundreds, even thousands of times, depending on image resolution and size. For example, a square image array of 512 pixels on a side such as will be presented here would require 512 repetitions of the sifting process, and each repetition would produce a complete component set and residue as outlined in (13.1). Once the component sets are obtained, they become the input to further processing steps that can produce unique products from the initial image. After a brief overview, these various products will be discussed, in turn, and examples used to illustrate the new possibilities opened up by the application of this robust technique to images.

13.2. Overview

Image processing in general has always made full use of available computer capabilities. Because of the shear size of the data to be analyzed, the needs of image

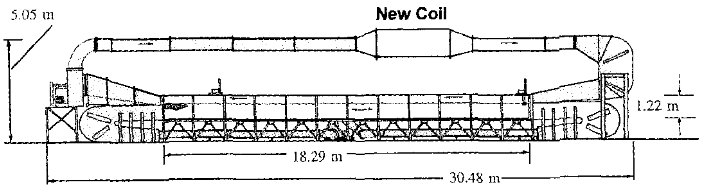

Figure 13.1: The wind, wave, and current interaction research tank at NASIRF.

processing have often "raised the bar" on hardware requirements, such as the need for more memory, increased computational speed, increased internal bus rates, and greater and better storage. Just as the images to be processed come from widely varied sources such as satellite imagery, aerial photography, microscope imagery, industrial imaging for quality control, and CT scan data for medical applications, so do the methods of image processing vary. It is almost always driven by a need to reveal or detect some feature within the image, to clarify the feature or resolution, or to make possible the measurement of a feature of the image, to name reasons why image processing is used. Therefore, image processing encompasses a wide range of mathematical techniques with a proven track record of effectiveness and established mathematical foundations.

The approach taken here is to refer the reader to well-established texts such as Castleman (1996) or Russ (2002) as a starting point in a vast literature already published on the subject, and to outline the new and important methods that can now be added to the available tools for producing new and unique image products. The descriptive and mathematical groundwork for this new approach has already been established in the series of articles denoted here as "foundation articles," by Long et al. (1995), Huang et al. (1998, 1999, 2000, 2001, 2003a, 2003b, 2004), and Wu and Huang (2004). Others have also made valuable contributions to this concept of image data decomposition, as can be seen in the work of Nunes et al. (2003).

13.3. The analysis of digital slope images

13.3.1. *The NASA laboratory*

The laboratory used for acquiring the images discussed in this section is the NASA Air-Sea Interaction Research Facility (NASIRF) located at the NASA Goddard Space Flight Center/Wallops Flight Facility, at Wallops Island, VA. The test section is 18.3 m long and 0.9 m wide, filled to a depth of 0.76 m of water, leaving 0.45 m for air flow if needed. The facility can produce wind- and/or paddle-generated waves over a water current in either direction, and its capabilities, instruments, and software have been described in detail by Long (1992, 1993, 2004) and Long and Klinke (2002). The basic facility is shown in Fig. 13.1, with an additional new feature, indicated as "New Coils," recently installed to control the temperature and humidity of a cooled air flow over heated water.

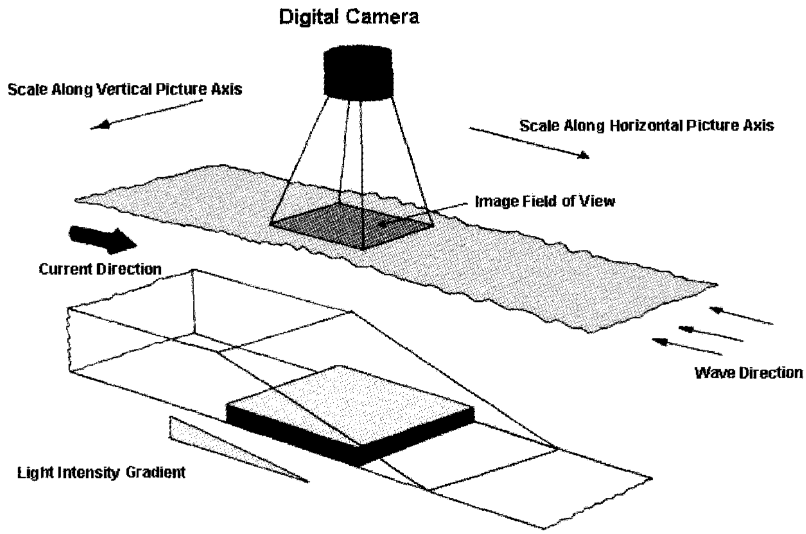

Figure 13.2: The digital slope imaging system at NASIRF, illustrating the false bottom used to create shear zones in the water current flow. A subsurface light source emits light with an intensity gradient along the direction of wave motion. The current flows against the waves over the false bottom in a depth of 38.1 cm, which increases down the slope of the full tank depth of 76.2 cm. Thus, the waves encounter increasing current strength until they are blocked. The pixel indices of the image area run as shown on the horizontal and vertical scales.

13.3.2. *The digital camera and set-up*

The device used to acquire the laboratory images presented here was a Silicon Mountain Design M-60 camera, capable of acquiring images of up to 1024 $\times$ 1024 pixels at a resolution of 4 096 intensity levels and at a rate of up to 60 images s^{-1}. For the examples shown here, the resolution was set at 512 $\times$ 512 pixels, at a rate of 60 images s^{-1}. The camera was mounted to look vertically down at the water surface, so that its 512 $\times$ 512 pixel image area covered a physical square on the water surface of 26.54 cm$\times$ 26.54 cm. Each pixel thus covered a square of about 0.518 mm each throughout the image area. To obtain an image array of surface slope values from each 512$\times$512 image, the configuration illustrated in Fig. 13.2 was used. The light source was mounted at the bottom of the tank and initially produced a uniform field of light. A thin film that varied in transparency between clear and black along the downwind direction was placed on top of the light source, resulting in a light intensity output that varied linearly with fetch. Because of this variation and the laws of refraction, each image acquired by the camera had the downwind surface slope at each pixel location on the surface recorded in the intensity level of that pixel in the image array. By using calibration lookup tables obtained through simple geometry and the application of Schnell's law of refraction, this intensity level was then converted to the down channel surface slope for each pixel, an array of 512 $\times$ 512 numerical values.

13.3.3. *Acquiring experimental images*

With this imaging system in place, steps were taken to acquire interesting images of wave blocking due to an opposing water current. This system is illustrated in Fig. 13.2, which shows the presence of a false bottom. A transparent window was placed over the light source and allowed the light source to function, while maintaining the slope of the false bottom for the water flow. When water flowed against the wave direction, an area of current shear was set up over the light box. As discussed in Long et al. (1993), waves can become trapped in such a shear zone and shift to higher frequencies in the absence of wind. To illustrate what happens, Figs. 13.3a–c present a series of images of this phenomena. Although the camera acquired images at 60 s^{-1}, only a selection from the sequence is shown here. To help our eyes see the images, the 4 096 levels of gray have been converted to a color variation. A horizontal line down channel is also included to mark an area of interest, where a very rapid development occurs during the time covered by these images. Even though $\frac{1}{60}$ s variations may seem to be rapid for a water surface, one gets the impression from these images that something is developing faster than the camera acquisition rate. The images obtained do, however, capture significant stages in this rapid development.

Using the horizontal line through the phenomena in image 127, Fig. 13.4a illustrates the detail contained in the actual array of data values. Fig. 13.4b shows a comparison of consecutive image slices at $\frac{1}{60}$ s steps, through the entire 9-image sequence of images, from 127 to 135. These are horizontal slices through the region of an interesting phenomena and show the complex changes that can occur in surface slope over a time period covering only $\frac{8}{60}$ s.

13.3.4. *Using EMD/HHT analysis on images*

From Fig. 13.4b, the slice from image 129 (image Fig. 13.3b) was processed following the EMD sifting procedures, and the results are shown in Fig. 13.5, which shows that the complex surface may be represented by comparatively few components. The sifting was done via the extrema approach discussed in the foundation articles and produced a total of eight components, the first seven of which are shown in Fig. 13.5.

13.3.5. *The digital camera and set-up*

Using the components illustrated in Figure 13.5, the next step with Hilbert–Huang transform (HHT) analysis produces a result that can be visualized as in Fig. 13.6a showing the contour plot of the result.

In Fig. 13.6a, a standing wave pattern can be seen between about 4 cm and 10 cm on the horizontal scale of the image slice. This pattern persists through many images preceding and following this moment in the sequence, and within the group of standing waves, different peaks take a turn at being the largest. Because they

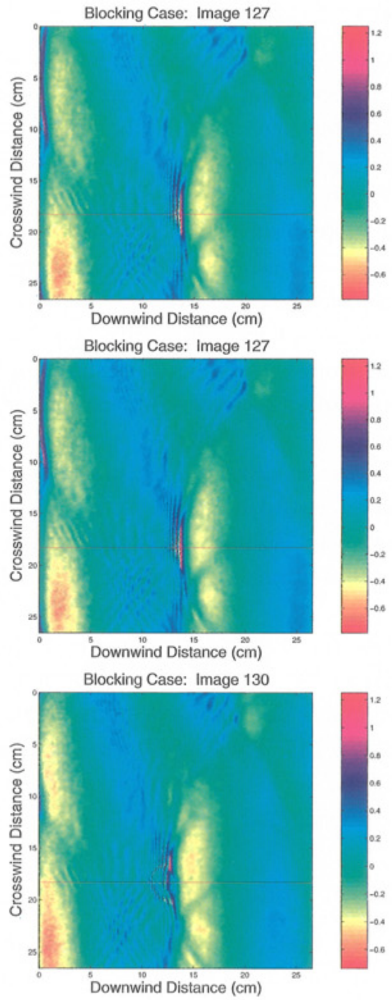

Figure 13.3: Wave blocking case. (a) Top. Current flows from left to right, and paddle waves move from right to left. The direction of the scale for downwind distance is an artifact of the matrix storage and indexing. The colorbar at right gives the slope intensity values. (b) Middle. Development continues at two time intervals after (a), or $\frac{1}{30}$ s later. The dark line along the direction of wave motion (right to left) shows the slice of data to be further processed. The current flows from left to right, and the colorbar at right shows the slope intensity. The downwind direction scale (horizontal) above is tied to the index of stored matrix elements and runs opposite to the wave direction. (c) Bottom. $\frac{1}{60}$ s later than (b). Note the structure extending down the face of the wave.

persist in time, however, they can be thought of as "standing waves" trapped in the blocking conditions of the current shear flow when the images were acquired. The shorter capillary wave group that appears on the leading edge of the crest and suddenly bursts out radially is represented in the higher values on the cm^{-1} scale.

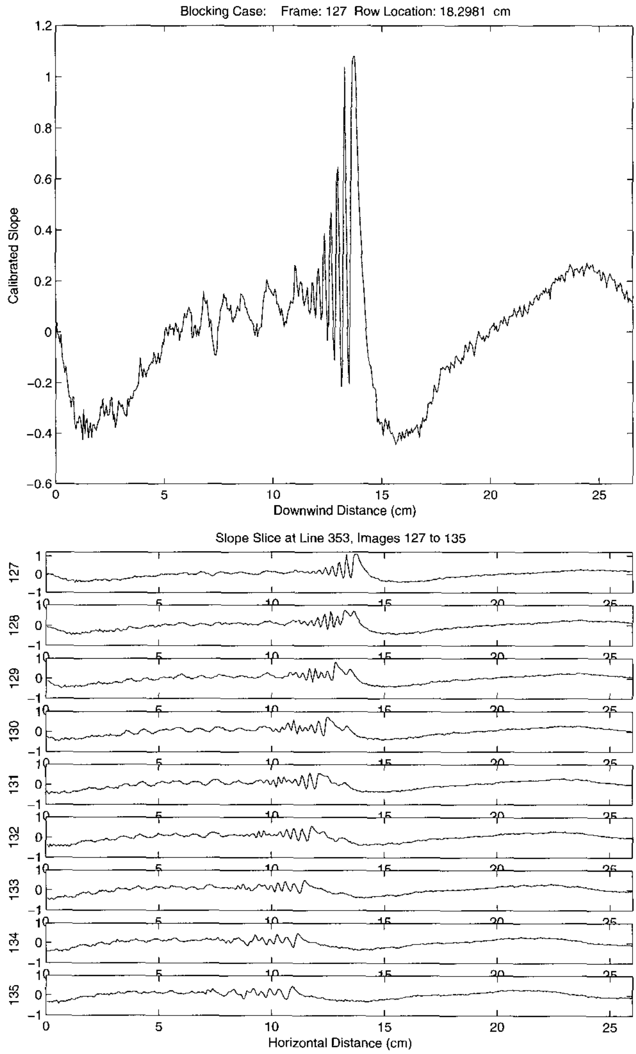

Figure 13.4: (a) Top. Horizontal slice at line 353 in Fig. 13.3a. (b) Bottom. Slices of slope at horizontal line 353 in images 127 to 135.

To produce a true wavenumber, one only has to convert by using

$$k = 2\pi/\lambda\,, \tag{13.2}$$

where k is the wave number (in cm^{-1}), and λ is the wavelength (in cm). The largest slopes occur where certain wavelengths are dominating in the data and its values are entered by the HHT process in the resulting array by location (horizontal location on the slice in cm), by wavelength inversed on the vertical (cm^{-1}) scale, and by amplitude or intensity of slope on the color scales.

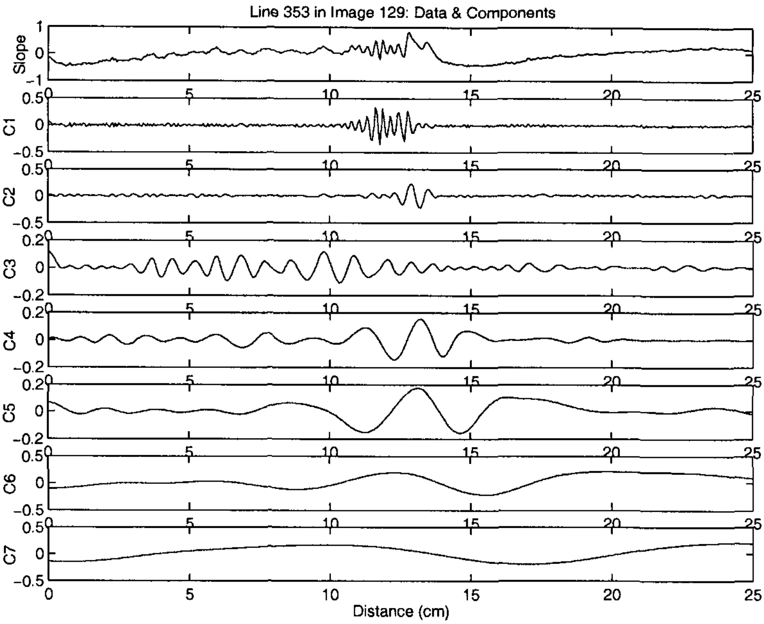

Figure 13.5: The horizontal slice of data at line 353 of image 129 in Fig. 13.3b, followed by the first seven components of EMD extrema sifting. Note the removal of intrinsic scales starting with the shortest (C1) and increasingly longer scales through C7.

To visualize how rapidly the capillary wave burst affects the result, a comparison is presented in Figs. 13.6b. It represents a combination of the result from the first and last images of the image sequence illustrated partially in Figs. 13.3a–c and 13.4a–b. By adding the result of image 127 to that of image 135, the change caused by the capillary wave burst, seen as a developing semi-circular feature on the leading edge of the wave, over a period of $\frac{8}{60}$ (0.1333) s can be seen. The standing wave pattern appears stable in the 5-to-11 cm horizontal area of the combined image in the vertical scale around 1 (cm^{-1}), while the incoming wave carrying the capillary wave's semi-circular burst is noted as moving left at a scale of 0.5 (cm^{-1}) from 15 to about 13 cm. Component wavelengths of the rapidly moving burst is seen in the vertical scales between 2 and 4.5 (cm^{-1}). By using the difference in horizontal distance covered by the burst in 0.1333 s, it can be shown that the burst is moving approximately 60 cm s^{-1} over the surface of an opposing, rapid flow. When the opposing current speed is also taken into account, this speed appears to be beyond the usual speeds of capillary waves of this wavelength.

13.3.5.1. *Volume computations and isosurface visualization*

Many interesting phenomena happen in the flow of time; thus, it is of interest to explain how changes occur in the images as time passes.

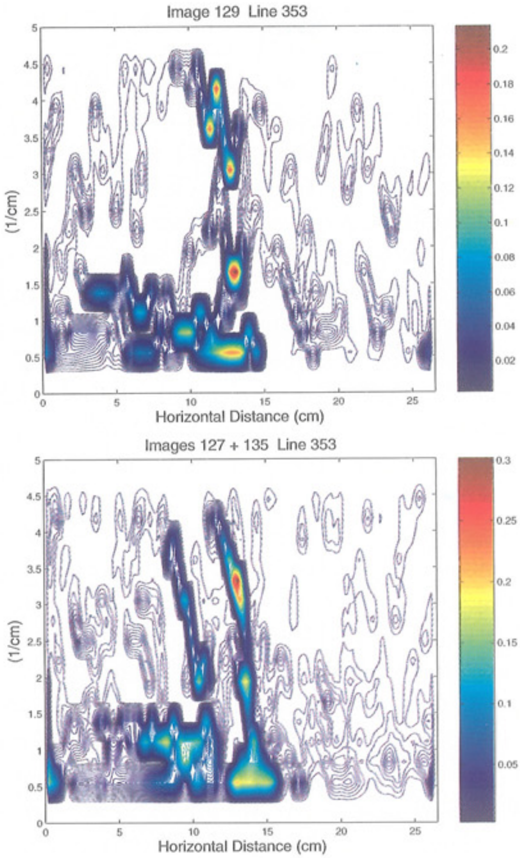

Figure 13.6: (a) Top. Contour plot of the results of EMD/HHT analysis on the slope slice taken horizontally from image 129, Fig. 13.3b. Note the standing wave pattern between 4 and 10 cm approximately, and the incoming wave at about 13 cm that is producing the burst of shorter waves appearing at 1.6, 3, 3.5, and 4.2 on the cm^{-1} inverse wavelength scale. Waves move from right to left into increasing current strength. The horizontal distance scale above is tied to the matrix elements, so that the waves progress through decreasing distance values. (b) Bottom. The analysis of the result of the sum of images 127 and 135. The standing wave pattern can be seen to be stable in the 5 to 11 cm horizontal area of the combined image, while the incoming wave carrying the capillary burst is noted as moving left at a scale of 0.5 (cm^{-1}) from 15 to about 13 cm. Above this, the rapidly moving burst is seen in the vertical scales between 2 and 4.5 (cm^{-1}).

By starting with a single horizontal line from the image, a contour plot as was shown in Figs. 13.6a can be computed from the EMD/HHT analysis. By using a longer set of images, such as from 110 to 150 (41 images covering $\frac{40}{60}$ or $\frac{2}{3}$ s), and a slice through the capillary wave's burst location, a set of 41 numerical arrays can be obtained from the EMD/HHT analysis. Each array can be visualized by means of a contour plot as shown before. The entire set of 41 arrays can now be combined in sequence to form an array volume, or an array of dimension 3. Within the volume, each element of the array contains the amplitude or intensity of the surface slope from the image sequence. One axis (call it x) of the volume represents the horizontal distance down the slice as before, in cm. Another axis (call it y) represents the resulting inverse length scale (cm^{-1}) that signifies the inverse wavelength of the slope values associated with waves in the data. The additional axis (call it z), produced by laminating the 41 arrays together, represents time, because each image was acquired in steps of $\frac{1}{60}$ s. Thus the position of the element in the volume gives location x (cm) along the horizontal slice, inverse wavelength (cm^{-1}) along the y axis, and time (s) along the z axis.

To visualize the data stored in a three-dimensional array, isosurface techniques are needed. This process could be compared to peeling an onion, except that the different layers, or spatial contour values, are not bound in spherical shells. After a value of slope amplitude or intensity is specified, the isosurface visualization will make transparent all array elements outside of the level of the value chosen, while shading in the chosen value so that the elements inside that level (or behind it) can not be seen.

Some examples of isosurface representations are seen beginning in Fig. 13.7a, where the horizontal line at 353 through the middle of the capillary wave's semi-circular burst splitting off the front face of the incoming carrier wave and then rejoining the standing waves around the 8 to 10 cm area. These occurances are the most energetic ones and are seen in the absence of lower levels. To illustrate the effect of the peeling level, a slow variation in peeling value is presented as Figs. 13.7a–d. At the peeling level of 0.03 shown in Fig. 13.7b, the incoming wave packet is seen to start around the 14 cm area and to progress up and left, denoting movement down the horizontal pixel line with time. As the burst to shorter wavelengths (larger cm^{-1} values) occurs, those slope intensity levels are taken by the capillary wave burst, which extends rapidly back along the cm^{-1} axis, and then return to the path taken by the carrier wave packet around the 0.5 s vertical level. With a peeling level of 0.025 as shown in Fig. 13.7c, the standing wave area around 8 cm and 1.9 on the cm^{-1} scale now appears as a column along time, initially shifted toward a shorter wavelength (compressed) until it is enveloped by the incoming carrier wave and capillary wave burst extending out along the y axis (cm^{-1}) as the shorter wavelengths suddenly appear. Fig. 13.7d illustrates a peeling level of 0.02. Here the standing wave column finally emerges near the end of the sequence (0.66 s), as a combination of standing wave and incoming wave energy. Further details can also be seen of the effect the incoming wave packet has on the standing wave before being merged with it and the capillary wave burst it is carrying. Also, other standing waves around 4 cm and 6 cm make an appearance at various times at this intensity level. With further decreases in the peeling level, a point is reached where the outer surface grows so large and complex that it starts to hide the underlying features. Nevertheless, the sequence shown in Figs. 13.7a–d demonstrates what is now possible by applying EMD/HHT to images.

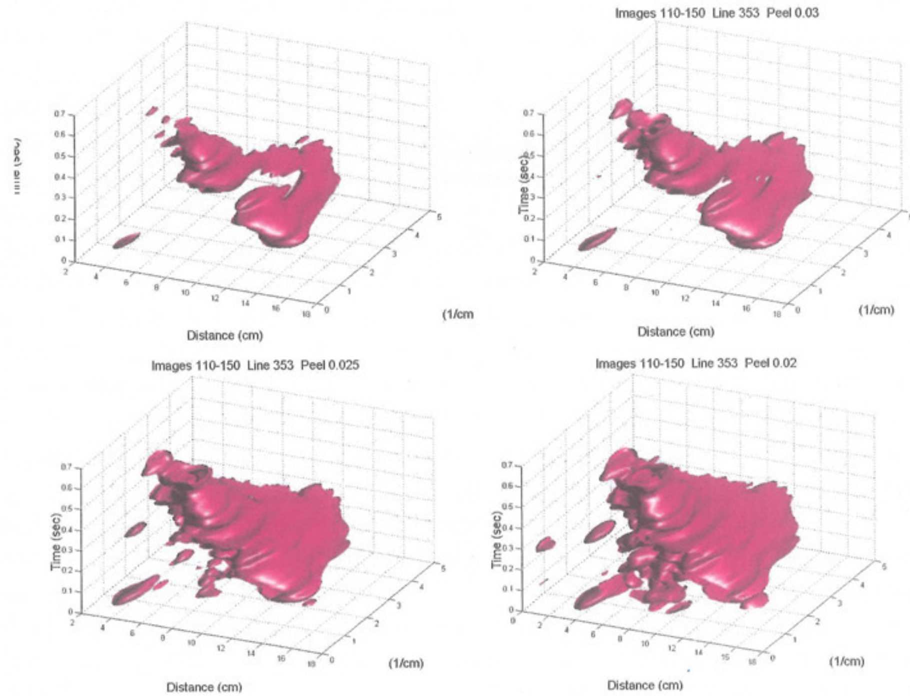

Figure 13.7: (a) Upper left. The result along the 353 through the center of the capillary wave burst from images 110 to 150. A fairly restrictive peel level (0.035) reveals details of the burst splitting off the front face of the incoming carrier wave and then rejoining the standing waves around the 8 to 10 cm area. (b) Upper right. Re-computing (a) for a peeling value of 0.03. The incoming carrier wave is seen around 14 cm. With the passage of time (up the z axis), the capillary wave burst extends the width to higher values along the y (cm^{-1}) axis. (c) Lower left. Peeling level now at 0.025, for (a) re-computed. Note the appearance of the stalk at coordinates of about 8 cm distance, 1.9 on the cm^{-1} scale. These coordinates correspond to a standing wave that was compressed by the approach of the incoming wave, bending to larger cm^{-1} values with the passage of time, and then being engulfed by the more energetic incoming wave and its capillary burst. (d) Lower right. Peeling level of 0.02, major details still evident. The combination of the incoming and standing wave column finally emerges near the end of the sequence (0.66 s), now moved to a slightly longer wavelength (smaller cm^{-1} value).

The example shown here was developed by using a single line from each image in the time sequence of images. Other approaches may be used as well, such as averaging over a subset of adjacent lines within each image, if doing so is justifiable based on the content of the image and the range of lines chosen over which to average. The process described here could also be repeated for each of the 512 lines across the wave tank of the present images, from top to bottom in each image, through the 41 images in the time sequence shown, or for even more lines by including more images. Doing so would produce an array with a dimension beyond 3, which would be no problem for the computers, but difficult for us to visualize. Each slice along the across tank axis from the higher dimensional array would be a volume result similar to the ones shown here, where isosurface techniques could reveal interesting processes and features.

Another approach for the analysis of images is to re-assemble the image components in a different way. Again starting with a single horizontal line, this time at line 256 through the center of the image, each center line from the sequence of images is laminated to its predecessor to build up an array that is 512 along one edge, in units of cm, and the number of images along the other axis, in units of time (s). Once complete, this two-dimensional array can be split into 512 slices along the time axis. Each of these time slices, representing the variation in slope with time at a single pixel location, can then be processed by using EMD/HHT techniques. For example, consider Figs. 13.8a–b. Fig. 13.8a represents the change in slope values at pixel 250 on line 353, or a location of 12.96 cm on the distance axis over a time period of just over seven seconds. Fig. 13.8b presents similar data, but at a location on line 353 at pixel location 300, or at a location of 15.55 cm. Both figures show the passage of wave groups of longer wavelength through the chosen pixel as a function of time. By using this data, the EMD/HHT techniques reveal variations in the frequency of the waves passing through this location. Consider Fig. 13.9a, which shows the change of frequency with time by using line 353 and pixel 250. Note the capillary wave bursts to higher frequency occurring very rapidly around the 1 s area, and also the persistent 2 Hz wave with fluctuating frequency. The sequence of images examined in earlier figures, images 110 through 150, occurs in time between 1.83 and 2.5 s, and the shorter 9 image sequence between 127 and 135 occurs on this time scale between 2.12 and 2.25 s.

By using the slope versus time data of Figs. 13.8a and 13.8b, EMD/HHT can be used to reveal the frequency variations, as shown in Figs. 13.9a and 13.9b, corresponding to the data of Figs. 13.8a and 13.8b, respectively.

Changes in curvature may also be examined by selecting two pixels along the same line. The spatial distance along this line between the pixels selected can be adjusted to vary the resolution and sensitivity to wavelength. The curvature along the direction of wave motion is then Δslope / Δseparation, where the change of slope is the difference between the two measured values at the two selected pixels, and the change in separation is the length difference along the chosen horizontal line between the two selected pixels. By repeating this procedure for each image in a sequence, the time variation of curvature at the selected location can be obtained and studied. This capability is another avenue opened up by the application of the EMD/HHT methods to images.

13.3.5.2. *Use of EMD/HHT in image decomposition*

Another application of EMD/HHT is a process similar to the filtering of images. A more accurate description of this process would refer to it as a separation of the complete image into component images, from the shortest scales to the longer scales. Again, as in the earlier analysis, the summation of these components produces the original data, in this case an image, with minimal computational differences from the original.

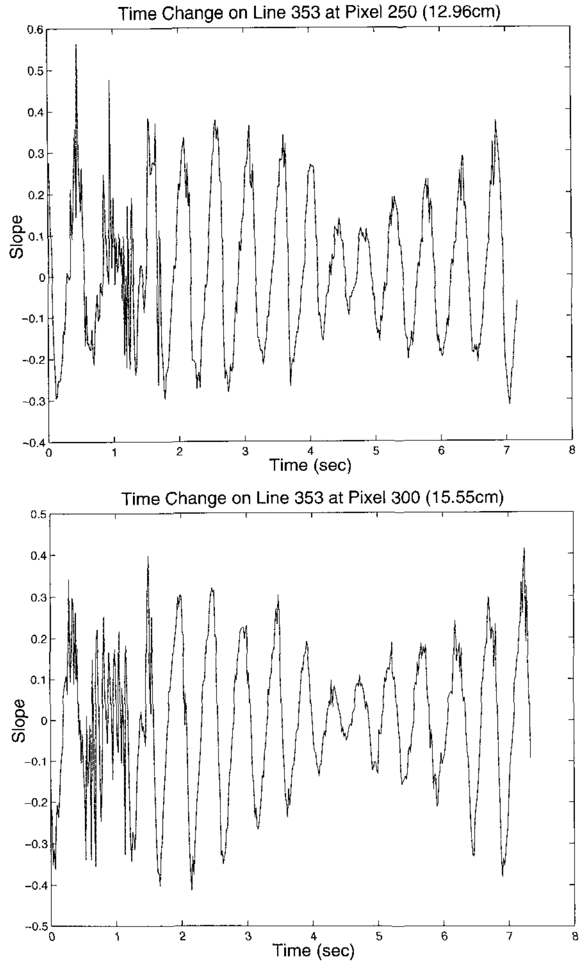

Figure 13.8: (a) Top. Change in slope over a time period of just over seven seconds at a location on line 353 through the burst at pixel 250 for a location at 12.96 cm. (b) Bottom. Same as (a), except through the burst at pixel 300, or 15.55 cm.

Starting with Fig. 13.3c, image 130 is again processed line by line, so that each horizontal slice produces a set of components. The difference in this approach is that now the first component is taken from each component set, or 512 different first components from the 512 complete sets. These 512 first components are laminated back together in the correct order, producing a 512 $\times$ 512 array, which can then be viewed as an image, the first component image. Fig. 13.10a shows the first component image of Fig. 13.3c. Note that only the shortest scales are seen, and in this case, they are the capillary wave burst seen in the earlier images. The decomposition (EMD) continues with Fig. 13.10b, illustrating that the slightly longer scale now resides with the incoming wave packet that carried and produced the capillary burst. Fig. 13.10c, the third component image, reveals the scales associated with

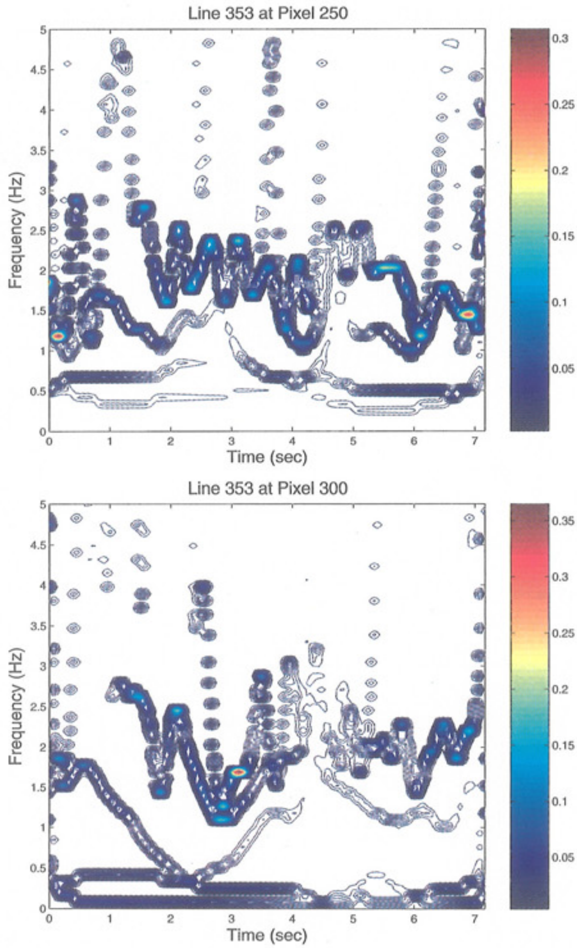

Figure 13.9: (a) Top. Change of frequency with time by using line 353 and pixel 250 from Fig. 13.8a. Note the bursts to higher frequency occurring very rapidly around the one-second area and also the persistent 2 Hz wave with fluctuating frequency. (b) Bottom. Same as (a), except now using pixel 300 from Fig. 13.8b.

the standing wave field, and it can be seen to project into the incoming wave, or put another way, the incoming wave has crossed into the domain of the standing waves. This result raises the possibility of the standing wave pattern being the trigger for the burst that arose out of a momentary but extreme steepness (slope > 1) on the incoming wave packet's front face near the crest. Fig. 13.10d shows the fourth component image containing the longer scale associated with the incoming wave, and some smaller contributions from the standing waves, along with an attachment to a bifurcation, seen in the top right quadrant. At this level, the lamination effects are becoming evident (some horizontal mismatch), illustrating the need for some matching computations between the slices at this and higher component levels. Up

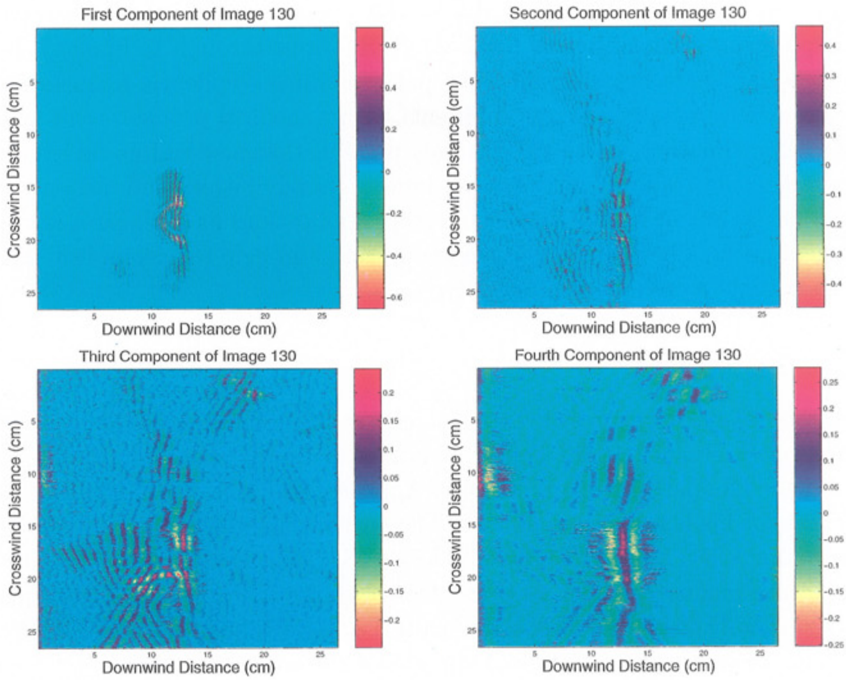

Figure 13.10: (a) Upper left. First component image from image 130 shown earlier, and assembled from the first components obtained from each of the 512 horizontal lines and slope data making up the image. Note that the shortest scale is present, and may be studied in the absence of all other scales. (b) Upper right. The next longer scale, the second component image from image 130, assembled as before, but now using the second component only. (c) Lower left. The third component image developed as before. Note the standing wave patterns now evident, and that the incoming carrier wave has now crossed into the area of the standing waves. (d) Lower right. The fourth component image, revealing the carrier wave scale and some of the persistent standing wave pattern. Note the apparent attachment to a bifurcation, seen in the top right quadrant. Lamination effects are becoming evident here (some horizontal mismatch), illustrating the need for some matching computations between the slices at this and higher component levels.

to now, the raw result of processing has just been assembled back together to form the image array.

13.4. Summary

As has been illustrated here, the application of the EMD/HHT techniques to image processing opens up new and exciting frontiers in image analysis. It is hoped that this brief review of some of these new possibilities will raise still others in the minds of readers, as well as point to new and interesting applications.

Images of water waves were used here because they happen to be the author's research field of interest. However, this present study in no way limits the wide application of the steps and results discussed here to interesting images of other processes. The new views into the complex interactions occurring routinely at the interface between the atmosphere and earth's oceans were made possible entirely by the power and versatility of the EMD/HHT breakthrough technology. If data from irregular heart beats, brain wave patterns during epileptic seizures, images from CT, MRI, or x-ray images of patients with a medical problem were analyzed by researchers in other fields, it is certainly possible that new and useful results and techniques would result. That work has indeed already begun, and not only in the medical fields, but in science and engineering applications as well. Such is the case with useful tools. They can simplify existing tasks and help to accomplish new ones that we thought were not even possible.

Acknowledgments

The author wishes to express his continuing gratitude and thanks to his colleague Dr. Norden E. Huang, Senior Fellow at NASA Goddard Space Flight Center, Director of the Goddard Institute for Data Analysis, and inventor of the EMD/HHT techniques for his help and discussions. The author also wishes to acknowledge and sincerely thank Dr. Dean G. Duffy of NASA/GSFC for his discussions on improvements to the manuscript and its presentation. Support from NASA Headquarters is also gratefully acknowledged, specifically Dr. Eric Lindstrom and Dr. William Emery, for their encouragement and support of the work.

References

Castleman, K., 1996: *Digital Image Processing*. Prentice Hall, 667 pp.

Huang, N. E., Z. Shen, S. R. Long, M. C. Wu, H. H. Shih, Q. Zheng, N.-C. Yen, C. C. Tung, and H. H. Liu, 1998: The empirical mode decomposition and the Hilbert spectrum for nonlinear and non-steady time series analysis. *Proc. R. Soc. London, Ser. A*, **454**, 903–995.

Huang, N. E., Z. Shen, and S. R. Long, 1999: A new view of water waves – The Hilbert spectrum. *Annu. Rev. Fluid Mech.*, **31**, 417–457.

Huang, N. E., H. H. Shih, Z. Shen, S. R. Long, and K. L. Fan, 2000: The ages of large amplitude coastal seiches on the Caribbean coast of Puerto Rico. *J. Phys. Oceanogr.*, **30**, 2001–2012.

Huang, N. E., C. C. Chern, K. Huang, L. W. Salvino, S. R. Long, and K. L. Fan, 2001: A new spectral representation of earthquake data: Hilbert spectral analysis of Station TCU129, Chi-Chi, Taiwan, 21 September 1999. *Bull. Seism. Soc. Am.*, **91**, 1310–1338.

Huang, N. E., M. C. Wu, S. R. Long, S. S. P. Shen, W. Qu, P. Gloersen, and K. L. Fan, 2003a: A confidence limit for empirical mode decomposition and Hilbert spectral analysis. *Proc. R. Soc. London, Ser. A*, **459**, 2317–2345.

Huang, N. E., M.-L. C. Wu, W. Qu, S. R. Long, S. S. P. Shen, and J. E. Zhang, 2003b: Applications of Hilbert–Huang transform to non-stationary financial time series analysis. *Appl. Stoch. Model. Bus.*, **19**, 245–268.

Huang, N. E., Z. Wu, S. R. Long, K. C. Arnold, K. Blank, and T. W. Liu 2004: On instantaneous frequency, *Proc. R. Soc. London, Ser. A*, under revision.

Long, S. R., R. J. Lai, N. E. Huang, and G. R. Spedding, 1993: Blocking and trapping of waves in an inhomogeneous flow. *Dynam. Atmos. Oceans*, **20**, 79–106.

Long, S. R., N. E. Huang, C. C. Tung, M.-L. C. Wu, R.-Q. Lin, E. Mollo-Christensen, and Y. Yuan, 1995: The Hilbert techniques: An alternate approach for non-steady time series analysis. *IEEE GRSS Newsletter*, **3**, *6–11.*

Long, S. R., and J. Klinke, 2002: A closer look at short waves generated by wave interactions with adverse currents. *Gas Transfer at Water Surfaces, Geophysical Monograph 127*, AGU, 121–128.

Nunes, J. C., Y. Bouaoune, E. Delchelle, N. Oumar, and Ph. Bunel, 2003: Image analysis by bidimensional empirical mode decomposition. *Image Vision Comput.*, **21**, 1019–1026.

Russ, J. C., 2002: *The Image Processing Handbook.* CRC Press, 732 pp.

Wu, Z., and N. E. Huang, 2004: A study of the characteristics of white noise using the empirical mode decomposition method. *Proc. R. Soc. London, Ser. A*, **460**, 1597–1611.

Steven R. Long
NASA/GSFC/WFF, Ocean Sciences Branch, Code 614.2, Wallops Island, VA 23337, USA
Steven.R.Long@nasa.gov